Spatiotemporal variations and relationships of aerosol-radiation-ecosystem productivity over China during 2001–2014

Wenhao Xue [a], Jing Zhang [a,*], Yan Qiao [a], Jing Wei [a,b], Tianwei Lu [a], Yunfei Che [a,c], Yulu Tian [d]

[a] College of Global Change and Earth System Science, Beijing Normal University, Beijing 100875, China
[b] Department of Atmospheric and Oceanic Science, Earth System Science Interdisciplinary Center, University of Maryland, College Park, MD, USA
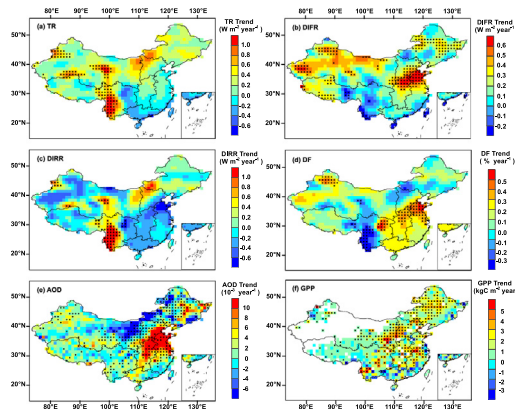[c] State Key Laboratory of Severe Weather & Key Laboratory for Cloud Physics, Chinese Academy of Meteorological Sciences, Beijing 100081, China
[d] Shaanxi Key Laboratory of Earth Surface System and Environmental Carrying Capacity, College of Urban and Environmental Sciences, Northwest University, Xi'an 710127, China

HIGHLIGHTS

- The Fu-Liou radiation transfer mechanism model showed excellent performance in estimating total and diffuse radiation in China;
- Aerosols have weakened the brightening of China due to the negative forcing on direct radiation;
- Although aerosol causes a diffuse fertilization effect, GPP is still lost in part due to high levels of aerosol loading in most areas of China.

GRAPHICAL ABSTRACT

ARTICLE INFO

ABSTRACT

Several air pollution episodes occurred in China in the past decade, and high levels of aerosols load also caused the changes of radiation, which could further influence the gross primary productivity (GPP) in the terrestrial ecosystem. This paper focuses on the spatiotemporal variations and relationship of aerosol-radiation-GPP in China during a heavy pollution period (2001–2014). For this purpose, the Fu-Liou radiation transfer mechanism model was used to estimate total radiation (TR) and diffuse radiation (DIFR) at the spatial resolution of $1° \times 1°$ based on the satellite aerosol optical depth (AOD) and other auxiliary data. This model shows excellent performance with an R^2 of 0.88 and 0.79 for TR and DIFR, respectively. A significant increasing trend (0.23 W m^{-2} year^{-1}) in TR was found in China in this phase, and it was mainly attributed to DIFR. Furthermore, a scenario without aerosols (AOD = 0) was simulated as a comparison to quantify the aerosol radiative forcing, which indicated that aerosols play a catalytic role in DIFR, increasing it by approximately 19.55%. Despite all this, aerosols have weakened the brightening of China due to the negative forcing on direct radiation. Meanwhile, 0.65–4.20 kgC m^{-2} year^{-1} increase of GPP was also captured in seven regions of China during this phase. However, the significant negative response of GPP to aerosol was found in most ecosystems in the growing season of vegetation, and the highest correlation of -0.76 ($p < .01$) existed in the central China forest regions. It suggests although aerosol causes a diffuse fertilization effect, GPP is still lost due to high levels of aerosol load in most areas of China during growing season of vegetation. This paper aims to determine the relationship among the aerosol-

* Corresponding author.
  E-mail address: jingzhang@bnu.edu.cn (J. Zhang).

radiation-ecosystem productivity in different regions of China, which could provide a reference for the divisional strategy formulation and classification management in different ecosystems.

1. Introduction

Solar radiation is an essential energy source for biogeochemical processes in the natural world, which play a crucial role in the energy and material cycles of earth systems. The observation of surface radiation is of great significance in understanding climate change and global warming. Therefore, the radiation parameters, including direct radiation (DIRR), diffuse radiation (DIFR), clearness index and diffuse fraction (DF), have been measured in China since the mid-20th century (Che et al., 2007). Based on those datasets, many previous studies have focused on long-term spatiotemporal variations in radiation to understand the trends and influencing mechanisms of radiation (Zhang et al., 2015; Zou et al., 2016). In recent decades, a process from dimming to brightening existed in China (Tang et al., 2011). From 1961 to 1989 (darkening period), the surface solar radiation decreased rapidly, with trends of $-8.3\,\mathrm{W\,m^{-2}\,decade^{-1}}$; in contrast, approximately $2.1\,\mathrm{W\,m^{-2}\,decade^{-1}}$ upward trends were observed for 1989–2013 (brightening period) (Wang and Wild, 2016). After that, Zhou et al. (2018) used the dataset from 48 radiation sites to calculate the trends of surface radiation in five climatic regions of China from 1962 to 2015, which suggested a downward trend above $20\,\mathrm{MJ\,m^{-2}}$ per decade among five different climatic zones in this phase. However, most studies were based on site-measured radiation datasets, and serious spatial discontinuities and low spatial coverage brought limits to the adequate understanding of radiation in all of China. Fortunately, many approaches were established and used to map the radiation in China according to the relationship between radiation and meteorological variables. Radiation transfer mechanism models (Huang et al., 2009), empirical relationships (Fan et al., 2018), mechanisms/deep learning approaches (Fan et al., 2019;) and other statistical or satellite derived methods (Kaplan and Kaplan, 2020) are the four most widely used traditional methods to assess the radiation network. Several factors affect solar radiation, among which aerosols play an essential function (Zhang et al., 2020a).

Atmospheric aerosols, especially those with aerodynamic diameters of 0.01–10 μm, can seriously affect the cloud formation and atmospheric environment (Andreae and Rosenfeld, 2008; Tie and Cao, 2009; Wei et al., 2017; Wei et al., 2018), and do huge damage to human health (Wei et al., 2019e, 2019f, 2020). In recent years, with the development of urbanization and industrialization, a quantity of aerosols has been released into the atmosphere, producing serious air pollution (Chan and Yao, 2008). Especially in the 21st century, the problem of air pollution has been an urgent national crisis in China. Aerosols can cause variations in solar radiation due to their absorbing and scattering effects. The IPCC Fifth Assessment report indicated that radiation forcing decreased by approximately 0.9 (1.9–0.1) $\mathrm{W\,m^{-2}}$ due to the reduction in aerosols at the global scale, which is conducive to reducing global warming (Stocker et al., 2013). This impact mainly depended on the type, mixing states and optical properties of particles (Chandra et al., 2004; Keppelaleks and Washenfelder, 2016). Zhang et al. (2018) found a significant aerosol direct radiative forcing in southern China from 2001 to 2016, and this effect was most noticeable in 2007, at $-24.75\,\mathrm{W\,m^{-2}}$. A decreasing trend in this effect was captured in this phase, with downward trends of $4\,\mathrm{W\,m^{-2}}$ per year. The results confirm that aerosols can significantly increase DIFR and reduce DIRR.

Terrestrial ecosystems are very sensitive to climate change (Chen et al., 2020; Qu et al., 2020; Zhang et al., 2020b), and the ecosystem functions are directly influenced by the radiative forcing of aerosols. Several studies indicated that the proportion of DIFR in total radiation (TR) could increase due to the radiative forcing of aerosols, results in the enhancement of photosynthesis of vegetation, which is called the diffuse fertilization effect (Osullivan et al., 2016; Williams et al., 2016; Unger

et al., 2017). However, due to the differences in aerosol composition, the responses of ecosystem functions to aerosols are also varied. Sulfate aerosols could promote photosynthesis of vegetation (Gu et al., 2003). Similarly, secondary organic aerosols oxidized from volatile organic compounds (VOCs) could also increase the net primary productivity (NPP) in ecosystem (Rap et al., 2018). In contrast, the GPP and NPP might decrease by aerosols generated from wildfire due to the enhancement of atmospheric absorption, the improvement of atmospheric stability, and the intensification of regional drought, which eventually cause soil water disturbance (Yue et al., 2017; Yue and Unger, 2018). Moreover, the ecosystem environmental variables, e.g., temperature, humidity and evaporation, could also be affected by aerosols, and those changes would eventually impact GPP (Moazenzadeh et al., 2018; Jiang et al., 2019). These influences also show obvious heterogeneity due to the leaf area index, canopy configuration, vegetation type and growing environment (Cheng et al., 2015; Niyogi et al., 2004). However, aerosol-radiation-ecosystem productivity studies are still insufficient in China, and the majority of that research is based on in-situ-measured radiation. Therefore, it is extremely indispensable to establish a radiation network and quantify the impact of aerosols on the radiation in different regions of China, which benefits by completely acknowledging the relationship among aerosol-radiation-ecosystem productivity.

This paper attempts to use the Fu-Liou radiation transfer mechanism model, which owns a complete set of parameterization schemes for cloud optical properties, combined with the Moderate Resolution Imaging Spectroradiometer (MODIS) aerosol optical depth (AOD), Clouds and the Earth's Radiant Energy System (CERES) cloud and other auxiliary data to estimate the radiation in China during the heavy pollution period (2001–2014). After that, a scenario without aerosols is simulated as a comparison to quantify the aerosol radiative forcing. In addition, the spatiotemporal variations and relationship of aerosol-radiation-GPP are described in this paper, and the sensitivity of different types of ecosystems to radiation and aerosol are assessed as well. This paper aims to determine the relationship among the aerosol-radiation-ecosystem productivity in different regions of China, which could provide a reference for the divisional strategy executer and classification management in different ecosystems.

2. Study area and dataset

2.1. Study area

The spatiotemporal variations and relationship of aerosol-radiation-GPP in China are analyzed in this paper. Due to the different geographical locations, significant differences in radiation existed within mainland China. Therefore, China was divided into seven regions (Fig. 1): northeastern, northern, eastern, southern, central, northwestern and southwestern China; these areas are abbreviated NEC, NC, EC, SC, CC, NWC and SWC, respectively (Ding et al., 2007), in this paper. The municipalities, provinces and autonomous regions contained in each region are shown in Table S1. Due to the special climate characteristics of the Inner Mongolia autonomous region, this area was divided into three parts, which severally belong to NEC, NC and NWC.

2.2. Datasets

2.2.1. MODIS AOD data

Two traditional algorithms, i.e. dark-target (DT) algorithm and deep-blue (DB) algorithm were widely used to generate the MODIS aerosol products. It has been found that the retrievals of DB aerosol products showed better performance than DT aerosol products,
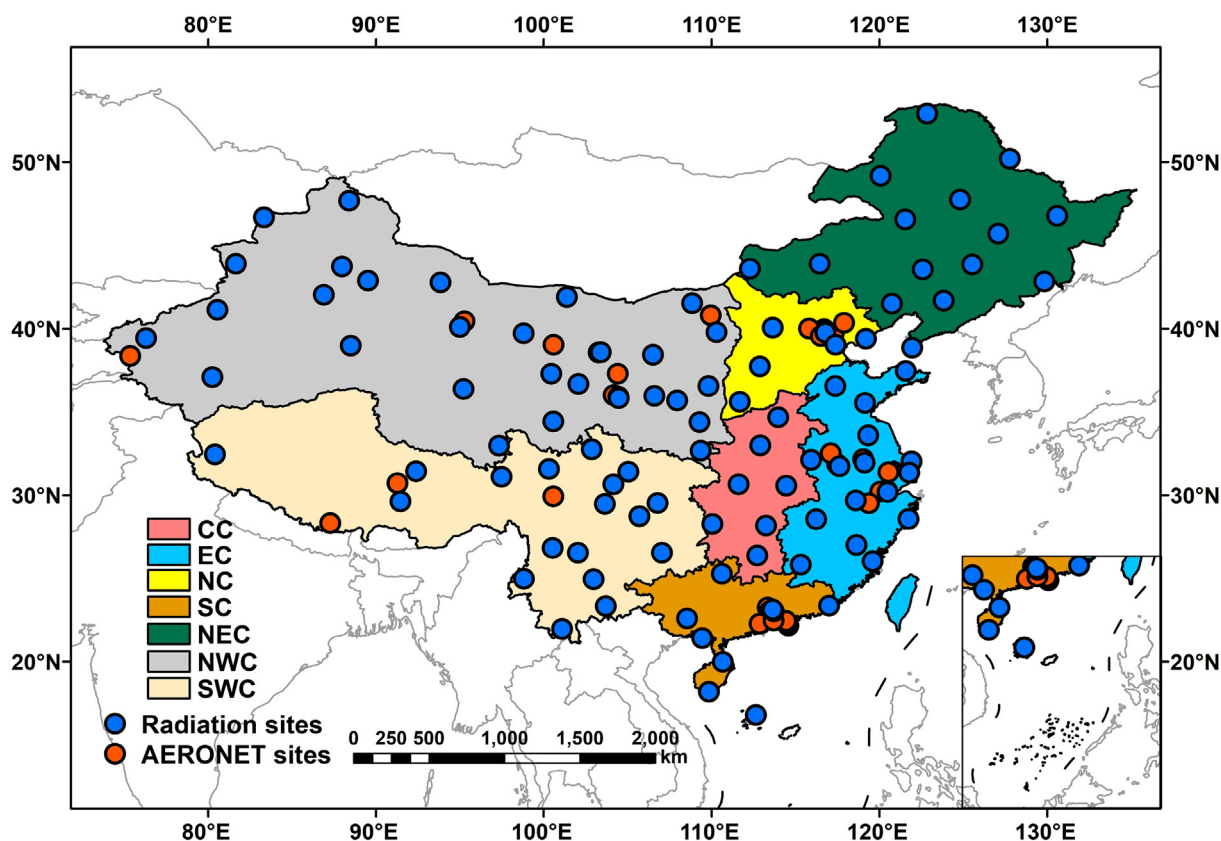
Fig. 1. The spatial distribution of China meteorological administration (CMA) radiation and aerosol robotic network (AERONET) AOD sites, and the seven study areas are also shown.

especially over bright urban surfaces (Wei et al., 2019c, 2019d). However, large numbers of missing values are exits in this dataset due to unfavorable observation conditions. To increase the data coverage, a combined DT and DB (DTB) dataset aerosol product was generated. The selection of DT or DB data in each grid depends on the normalized difference vegetation index (NDVI) in this gird. Where NDVI≤0.2, the DB data are used, and where NDVI ≥0.3, the DT data are selected. If the NDVI was between 0.2 and 0.3, the higher quality assurance (QA) flag aerosol data is selected, and if both return QA = 3 for DT and DB data, the mean value is used (Sayer et al., 2014). In this paper, the MODIS collection 6.1 (C6.1) Level 3 DTB AOD product was selected, with the temporal and spatial resolution of daily and 1° × 1° (Sayer et al., 2019; Wei et al., 2019a, 2019b). Compared with some old version aerosol products (collection 6 and collection 5.1), the latest C6.1 aerosol products has improved the retrievals of both DT and DB AOD based on the update of surface reflectance (Hsu et al., 2019; Wei et al., 2019c). The quality assurance flags were used to represent the accuracy for MODIS AOD retrievals product, which ranges from 3 (high) to 0 (low) (Levy et al., 2010). And the highest quality AOD products are used in our study. Those products are captured by two satellites, i.e., Terra and Aqua, and the Terra AOD (MOD 08) was used to calculate the surface radiation for ante meridiem in this paper, while Aqua AOD (MYD08) was used for post meridiem. In addition, the monthly mean AOD was obtained to analyze the relationship of aerosol-radiation-GPP. However, several missing data points were caused by the satellite and cloud features in China. Therefore, we first combined the Terra and Aqua daily DTB AOD retrievals at 550 nm to increase the spatial coverage. The combined AOD shows the excellent consistency compared with the AOD measured at AERONET sites (Fig. 1), with the correlation coefficient R^2 of 0.73, and it is described in detail in our previous study (Xue et al., 2020). In addition, the records that reported fewer than six times for each month have been removed to prevent accidental errors caused by missing data (Hsu et al., 2013).

2.2.2. CERES cloud data

In this paper, the optical parameters of cloud-ice and cloud-water were calculated according to seven cloud characteristics: cloud-water content, effective radius of cloud water particles (ERCWP), cloud-ice content (CIC), effective scale of cloud ice particles, cloud top height, cloud bottom height and cloud fraction. Those datasets were sourced from the CERES-SYN Edition 3a Level 3 products (Doelling et al., 2013). The spatial and temporal resolutions of the cloud data were 1° × 1° and 3 h, respectively. In addition, the cloud data were divided into four layers according to the top pressure, i.e., high cloud (<300 hpa), low cloud (>700 hpa), higher middle cloud (300–500 hpa) and lower middle cloud (500–700 hpa).

2.2.3. Other auxiliary data

Three profiles of meteorological parameters sourced from National Centers for Environmental Prediction (NCEP)/National Centers for Atmospheric Research (NCAR) were selected in this study, and include pressure, temperature and humidity (Kalnay et al., 1996). Moreover, the MODIS MCD43C3 surface albedo product (Schaaf et al., 2002) was also input into the Fu-Liou model. In addition, the Modern-Era Retrospective Analysis for Research and Applications, version 2 (MERRA-2) aerosol composition products (Gelaro et al., 2017) were also used as input data to represent the aerosol composition in the Fu-Liou model. The proportion of seven aerosol types was provided by this product, including organic carbon, black carbon, sulfate, coarse- and fine-mode dust and sea salt. After that, the bilinear interpolation was used to interpolate all datasets to the same spatial resolution of 1° × 1° as AOD.

2.2.4. Radiation data

The situ-measured radiation dataset from 2001 to 2014 sourced from the China Meteorological Administration (CMA) was used in this paper to verify the accuracy of the Fu-Liou model. Before that, we

screened out 99 CMA sites, which have effective records of more than one third, to reduce the error caused by data loss. Among all sites, only 12 sites provided the diffuse radiation measurements. The average of the daily radiation for one month was taken as the monthly mean radiation in this study. The spatial distribution of all sites is shown in Fig. 1. In general, the distribution of CMA radiation stations in China is uniform, and can be used to evaluate the radiation simulation results of different regions in China.

2.2.5. GPP and ecosystem type data

To explore the relationship among aerosol-radiation-GPP, the MODIS GPP data (MOD17A2H) were employed in this paper. Excellent inversion accuracy for this product has been described by Steve et al. (2015), and the temporal and spatial resolutions of these data were 8 days and 500 m, respectively. Similar to other input data, the GPP was also interpolated to the spatial resolution of $1° \times 1°$ according to the bilinear interpolation. Similar to the aerosol products, the highest quality products were used in this paper. To further determine the relationship of aerosol-radiation-GPP in China, the ecosystem type data were also applied in this study. The ecosystem type data were collected from the Resource and Environment Data Cloud Platform at a spatial resolution of 1 km. Seven ecosystem types, including farmland, forest, grass, urban, water and wetland, urban desert and bare land, are classified in this product. However, due to the sample number limits, we only used the ecosystem types of farmland, forest and grass for the analysis. Fig. S1 shows the proportion of ecosystem types in different regions. In general, the grass ecosystem accounts for the highest proportion in China, accounting for 32%, and it is especially the case in SWC (49%). The forest ecosystem is dominant in NEC, SC and CC, accounting for 35%, 64% and 45%, respectively. In contrast, the main ecosystem type is farmland in NC and EC, and the proportion for both is 43%. In addition, due to the whole coverage of the Taklimakan Desert in NWC, other ecosystems account for the greatest area in this region, up to 53%.

3. Methods

3.1. Fu-Liou model

The Fu-Liou model, which was modified by Kato et al. (2005), combined with the above input data, was used to construct the network of total radiation (TR), diffuse radiation (DIFR) and direct radiation (DIRR) in China from 2001 to 2014, at a temporal and spatial resolution of 3 h and $1° \times 1°$. We also calculated the diffuse factor (DF) according to the formula as follows:

$$DF = \frac{DIFR}{TR} \times 100\% \tag{1}$$

Fifteen bands of short wave (0.175–4.0 μm) and twelve bands of long wave (2200–10 cm^{-1}) could be calculated by this model. The radiation transmission scheme of delta-four-stream approximation was adopted in this paper to reduce the simulation error caused by clouds. This radiation transmission scheme can also capture the solar radiation under all-sky conditions. For the proportions of soot, insoluble aerosol, accumulated dust, coarse dust, sulfate aerosol, accumulated sea salt and coarse sea salt of the Fu-Liou model, the MERRA-2 data for black carbon, organic carbon, fine-mode dust, coarse-mode dust, sulfate, fine-mode sea salt and coarse-mode sea salt were adopted. We calculated the AOD of different aerosol types according to the formula as follows:

$$Aerosol\ type\ AOD = \frac{Aerosol\ type\ AOD_{MERRA-2}}{AOD_{MERRA-2}} * AOD_{MODIS} \tag{2}$$

After that, two optical parameters including single scattering albedo and asymmetry factor for total aerosol composition were calculated based on the optical properties of various aerosols set in Fu-Liou model, which are shown in Table S2. In addition, the aerosols are set as the externally mixed for Fu-Liou model. Moreover, the vertical distribution of aerosol was also set as the default exponential decline mode. In addition, a scenario without aerosols (AOD = 0) was assumed in this study, and the TR, DIFR, DIRR and DF under this scenario were also simulated to quantitatively analyze the influence of aerosols on radiation.

3.2. Statistical analysis

Based on the CMA monthly radiation data, many evaluation indexes, including linear regression equation (slope and intercept), Pearson correlation coefficient (R), mean absolute error (MAE) and root mean square error (RMSE), were established to verify the accuracy of Fu-Liou model. The statistical metrics were explained as follows:

$$MAE = \frac{1}{n} \sum_{k=1}^{n} | Radiatin_{Measure} - Radiation_{Model} | \tag{3}$$

$$RMSE = \sqrt{\frac{1}{n} \sum_{k=1}^{n} (Radiatin_{Measure} - Radiation_{Model})^2} \tag{4}$$

Among them, the R indicates the linear correlation between model and observation. The slope, intercept and MAE represent the overall estimation accuracy of this model, and the slope > 1 (slope < 1) indicates the overestimation (underestimation) of the Fu-Liou model. Moreover, the uncertainty of model simulation was expressed by RMSE. Then the ordinary least squares fitting method is selected in this paper to calculate the annual averaged linear trend of aerosol-radiation-GPP from 2001 to 2014. In addition, the correlation coefficient approach was also used to analyze the relationship among aerosol-radiation-GPP, and the paired-samples t-test was selected to evaluate the statistical significance.

4. Results and discussions

4.1. Model evaluation

Fig. 2 shows the density scatterplots of the monthly TR and DIFR simulations and measurements from 2001 to 2014 in China. To explore the applicability of Fu-Liou model in different ecosystems, the simulation results of the TR for farmland, forest and grass ecosystems (Fig. 2 (i-b)-(i-d)) and the DIFR for farmland, forest and urban ecosystems (Fig. 2(ii-b)-(ii-d)) were evaluated. The results illustrated that the Fu-Liou model had an excellent performance in simulating TR, with high R^2 values of 0.88, and low RMSE and MAE of 18.12 W m^{-2} and 21.35 W m^{-2}. However, this model appeared to slightly underestimate for TR, especially in the grass ecosystem, with the slope of 0.70 and RMSE of 29.51 W m^{-2}. In contrast, the best simulated performance was observed in the farmland ecosystem with the largest R^2 and slope values ($R^2 = 0.89$, slope = 0.80) and lowest simulation uncertainties (RMSE = 18.27 W m^{-2}, MAE = 20.08 W m^{-2}). This was mainly due to the difference of the surface albedo. High level of surface albedo could cause the multiple scattering between the sky and surface land, results in higher DIFR (Pinty et al., 2005). Furthermore, the radiative forcing of carbon aerosol is between 0.23 W m^{-2} and 0.16 W m^{-2} due to the influence of cloud cover and surface albedo (Penner et al., 1998). Additional, the different of aerosol types in several of ecosystems can also bring the uncertainty for model (Bassani et al., 2016). Similar to TR, the DIFR was also estimated most appropriately in the farmland ecosystem, which exhibited the highest correlation ($R^2 = 0.89$), the closest slope (0.97) and the lowest RMSE (9.95 W m^{-2}) and MAE (7.46 W m^{-2}) with measured DIFR. Remarkably, a slight overestimation was captured in the forest ecosystem, with the slope of 1.05. The
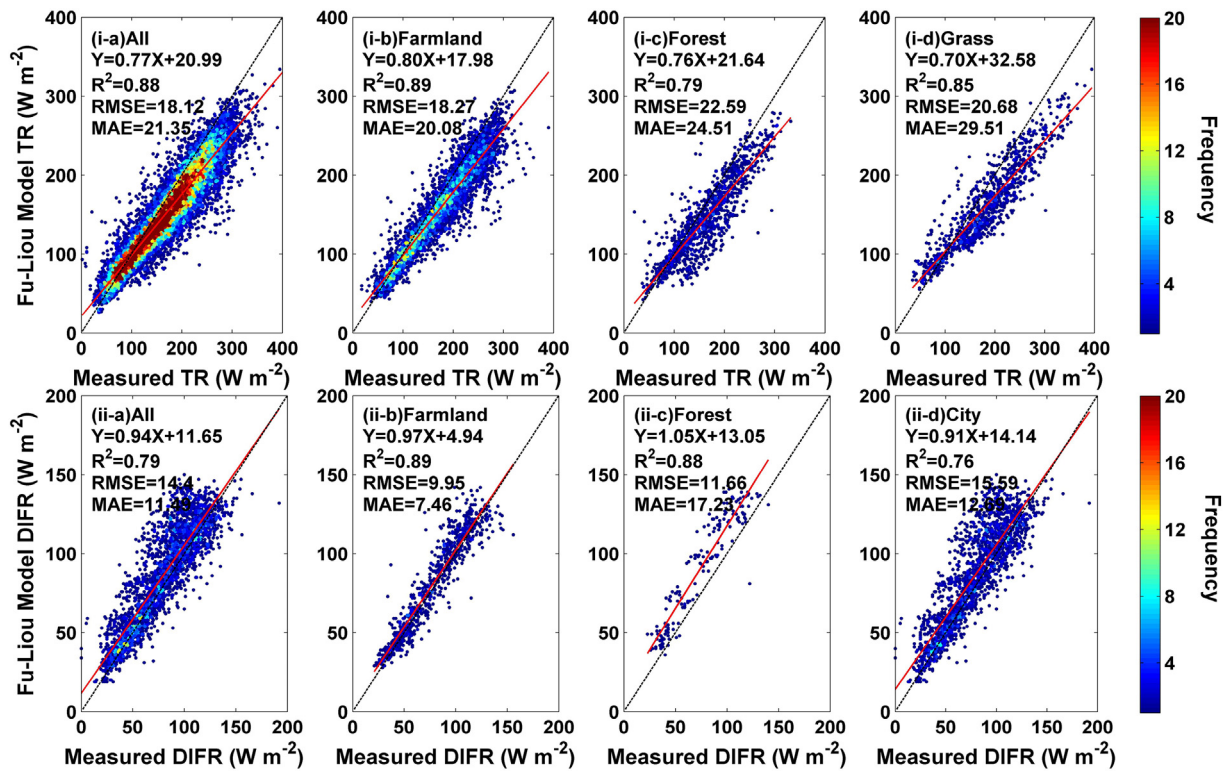
Fig. 2. Density scatterplots of the model simulated TR (i) and DIFR (ii) results for the Fu-Liou model at the monthly scale over China. The black dashed and red solid lines indicate the 1:1 line and the linear regression line, respectively. (For interpretation of the references to colour in this figure legend, the reader is referred to the web version of this article.)

simulation effect of the urban ecosystem was the worst, with the lowest slope (0.91) and R^2 (0.76) and the largest RMSE (15.59 W m^{-2}) and MAE (12.69 W m^{-2}). The aerosol optical properties and vertical distribution could also cause the uncertainty (Li et al., 2020).

In addition, significant difference existed in radiation simulating performance for various months. Fig. 3 shows the box plots for the monthly average radiation of the Fu-Liou model and CMA measurements in China for 2001–2014. The underestimation of TR mainly occurred from March to September, which was 13.90 W m^{-2}–35.34 W m^{-2}, especially in June, with the error of 14.5%. Moreover, obvious overestimation was captured for the results of DIFR simulation, which is one of the reasons for the underestimation of TR. This phenomenon mainly occurred in February, March, April and June, with the underestimation of 23.85%, 25.33%, 15.39% and 10.04%, respectively. Compared to the measurements, those errors were mainly attributed to the deviation of aerosol composition and radiation transmission scheme. In addition, the spatial interpolation of input data could also cause data uncertainty. Nevertheless, the radiation trends were accurately captured by the Fu-Liou model, and it can be applied to explore the spatiotemporal variation of radiation and analyze its potential impact in China.

4.2. Spatiotemporal trend in radiation, AOD and GPP

Fig. 4 shows the spatial distribution of radiation in China during 2001–2014. In general, the annual averaged TR among China was 156.18 W m^{-2}, contributed by 84.00 W m^{-2} for DIFR and 72.18 m^{-2} for DIRR. The highest DIFR and DIRR was captured in SWC and NWC, which was 91.49 W m^{-2} and 70.92 W m^{-2}, respectively. In contrast, the lowest was found in NEC and CC with the DIFR and DIRR of 72.89 W m^{-2} and 42.25 W m^{-2}, respectively. In addition, the higher DF was existed in SC (66.78%), EC (65.85%) and CC (64.77%) region. This is mainly due to the distribution of aerosols (Mahowald et al., 2011). The spatial distribution of AOD has also been calculated, and it

was similar to DIFR in most area of China. Due to its high-level industrialization and urbanization, the highest AOD occurred in CC, and the annual mean value was 0.73. Similarly, the AOD in EC, SC and NC were also at a high level, which was 0.69, 0.58, and 0.47, respectively. By contrary, the low aerosol loading existed in NEC (0.29), NWC (0.25) and SWC (0.25), where the anthropogenic activities were not as high as other regions. Furthermore, the spatial distribution of GPP was also shown in Fig. 4. The GPP in China gradually increased from the northwest to the southeast. And it was highest in SC, reaching 315.04 kgC m^{-2}.

Fig. 5 shows the temporal trends of radiation in China from 2001 to 2014. Before that, we compared the calculated TR and DIFR trends with the ground measured trends in this paper. The results indicated that the simulated TR showed the same trend with the measured TR, which was 0.23 W m^{-2} year^{-1} during this period in China. However, the simulated DIFR trend (0.38 W m^{-2} year^{-1}) was lower than the measured DIFR trend (0.67 W m^{-2} year^{-1}). The number of surface sites with DIFR measurement is only 12 in China, and they are mainly located in urban regions. High-speed development of urbanization and industrialization make aerosol loading increase rapidly, resulting in a faster growth trend for DIFR, which could cause significant uncertainty for the assessment of DIFR trend. Despite all this, the interannual variations are relatively consistent between simulations and measurements, which could also indicate the accuracy of Fu-Liou model. Moreover, the increase of DIFR resulted in the increasing trend of DF, which was approximately 0.16% per year. And the DIRR trend was −0.15 W m^{-2} year^{-1} among China during this phase.

Fig. 6 shows the spatial distribution of annual averaged radiation trends for the four radiation parameters in China from 2001 to 2014. However, there was obvious spatial heterogeneity in radiation trends. The most substantial increases of TR mainly occurred in SWC and NWC. The increase of DIFR was the main reason for the rise of TR. Significant upward trends for DIFR and downward trends for DIRR existed in NC. In contrast, those trends were polar opposites in SWC. Thus, the
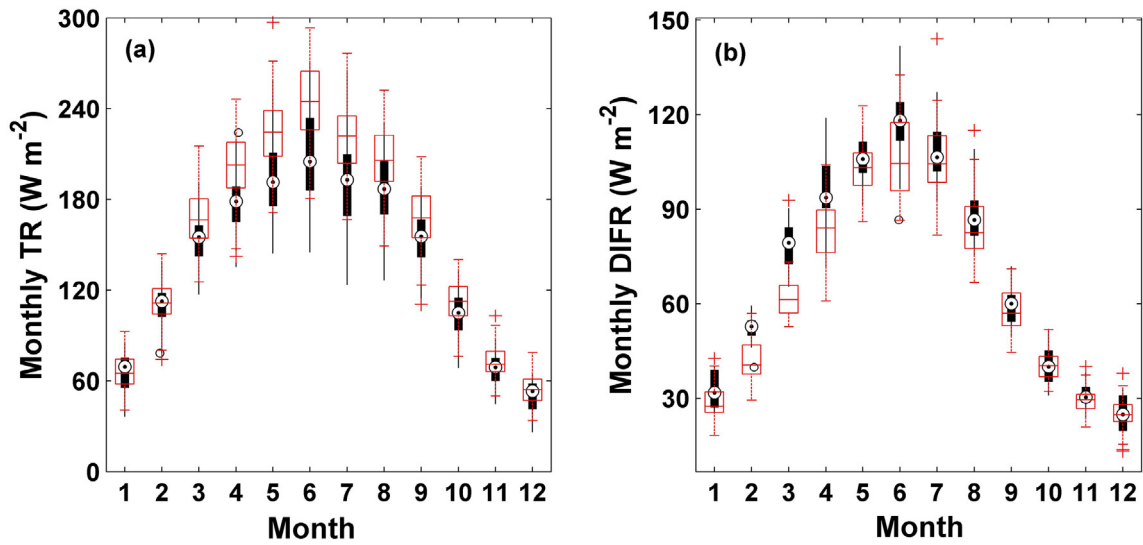
Fig. 3. The box plots of the monthly mean simulated and measured TR (a) and DIFR (b) in China from 2001 to 2014. The red boxes indicate the CMA measured radiation, and the black boxes represent Fu-Liou model simulated radiation. In the boxes, the upper and lower bands of red dashed and solid lines indicate the maximum and minimum radiation under the non-abnormal range. The top, bottom and center of the boxes represent 75%, 25% and 50% of values, respectively, and the crosses and circles are outliers. (For interpretation of the references to colour in this figure legend, the reader is referred to the web version of this article.)
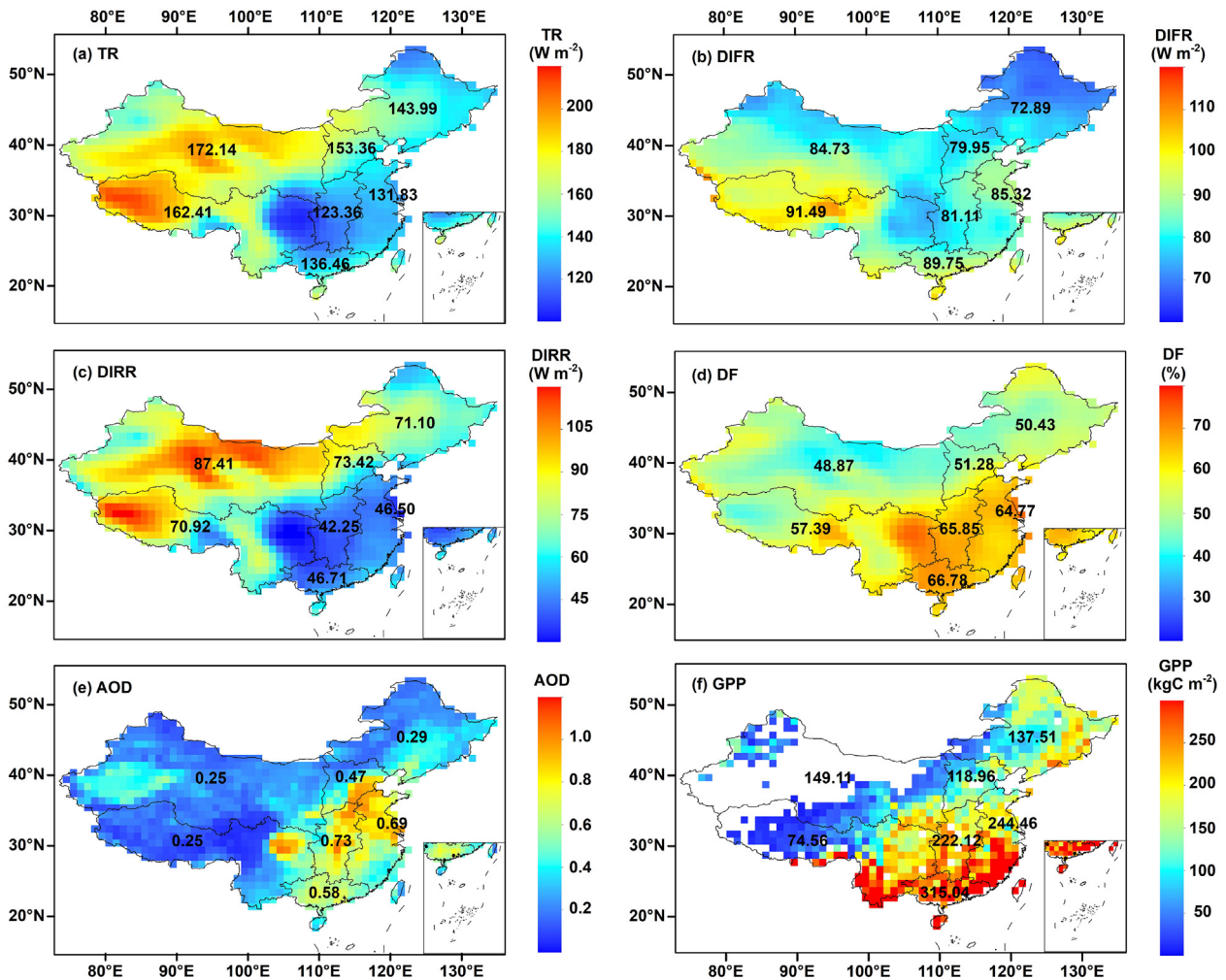

Fig. 4. The spatial distribution of TR (a), DIFR (b), DIRR (c), DF (d), AOD (e) and GPP(f) in China from 2001 to 2014.
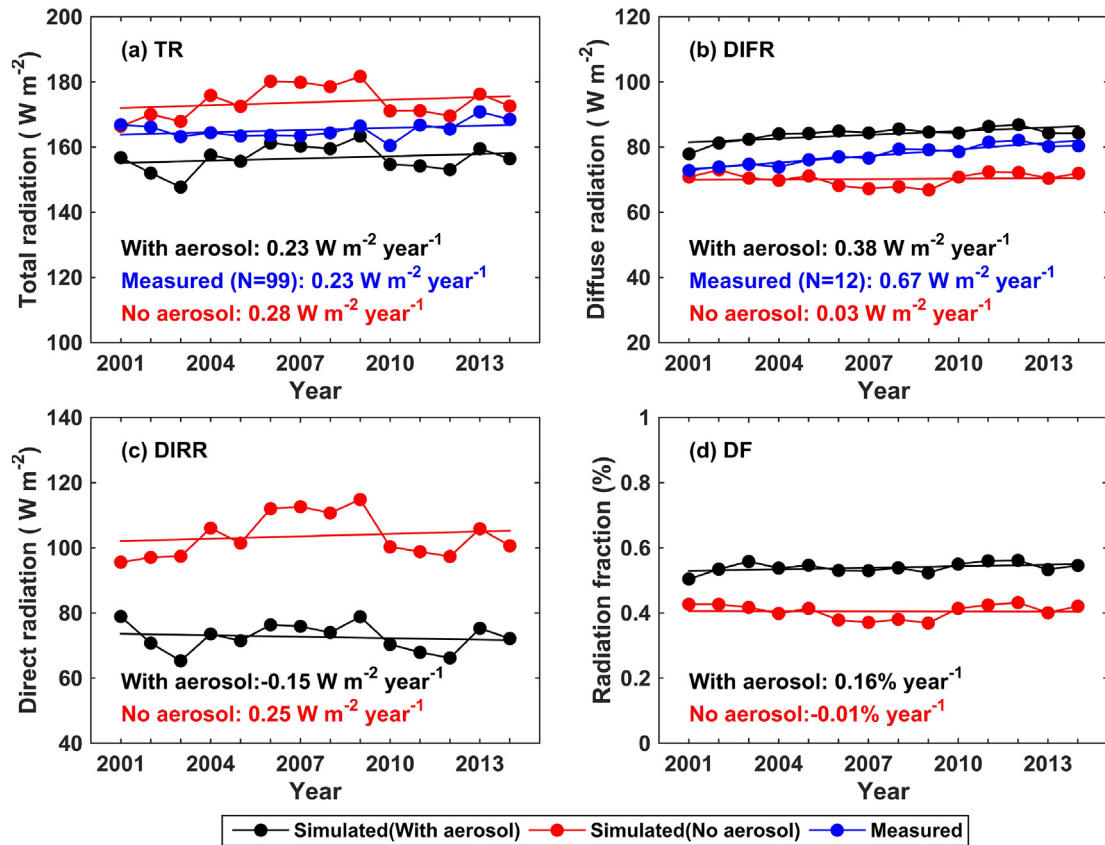
Fig. 5. The values and temporal trends of radiation parameters in the scenarios with aerosol (black lines) and no-aerosol (red lines) in China from 2001 to 2014: (a) TR; (b) DIFR; (c) DIRR and (d) DF. The surface measured values and temporal trends for TR (number of sites = 99) and DIFR (number of sites = 12) were also given (blue lines). (For interpretation of the references to colour in this figure legend, the reader is referred to the web version of this article.)

annual radiation trends in the seven regions were calculated separately to comprehensively obtain the variations in radiation among all of China.

Table 1 lists the average trends of radiation in different regions of China. Generally, all regions showed increases in DIFR, with the fastest uptrends of 0.34 W m^{-2} year^{-1} ($p < .1$) in the CC region. The slowest trends occurred in the SC region, with the uptrends of 0.04 W m^{-2} year^{-1} ($p > .1$). Similar uptrends existed in DF, and the trends were 0.00% - 0.28% per year for all regions. However, significant differences were found for the regional distribution in the temporal trends of DIRR. For the NEC, NC and SWC regions, a great increasing trend was captured, of 0.13–0.15 W m^{-2} per year. In contrast, a substantial downtrend trend was observed in the EC, SC and CC regions, which was −0.29 to −0.31 W m^{-2} per year. In addition, the DIRR in NWC was kept stable (trend = −0.00, $p > .1$). Due to the change of DIFR and DIRR, except for the EC and SC regions, the trends of TR in the other five regions increased, with upward trends in the range of 0.05 W m^{-2} year^{-1} to 0.38 W m^{-2} year^{-1}. Table S3 shows the radiation trends in seven regions under the no-aerosol scenario. In this scenario, the upward trend of DIFR also existed in most regions, with the increased trends of 0.03 to 0.21 W m^{-2} per year, which was significantly lower than the trends of aerosol scenario. In addition, the results indicated that the aerosol could cause the opposite trend of DIFR in NEC and SWC region. Furthermore, aerosols also result in retarding brightening, especially in NEC region, the trends of TR was in the range from 0.43 W m^{-2} year^{-1} to 0.30 W m^{-2} year^{-1}

However, the aerosol level in China had dramatically improved over the years. Fig. 6 also shows the spatial distribution of the annual trends of AOD and GPP in 2001–2014. In general, a significant increasing trend was captured during this phase, accounting for 65.8% of the total area of China, and the mean upward trend was 0.002 per year. However, the

spatial distribution of AOD trends varied on the local scale. More rapidly increasing trends were found in the NC, EC and CC regions, and the upward trends were 0.005 year^{-1} ($p < .1$), 0.008 year^{-1} ($p < .01$) and 0.009 year^{-1} ($p < .05$), respectively. High-level urbanization and industrial production lead to the increasing environmental burden in this region, especially for air pollution. Conversely, a significant downward trend was found in central Inner Mongolia, which was attributed to the implementation of policy on windbreak and sand-fixation in China. In addition, with the contribution of the 'Green Wall of China' in this area, most dust transport had been blocked (Tan et al., 2015). Furthermore, low-level industrialization and emissions of air pollutants were also helpful in the decreasing of AOD (Guo et al., 2011). The GPP trends increased overall in China, with the averaged upward trend of 1.17 kgC m^{-2} year^{-1} while the decreasing samples only accounted for 12.9% of all. For regional scales, except for a slight decreasing trend that occurred in SC, all regions had an upward trend (0.65–4.20 kgC m^{-2} year^{-1}). This trend was most significant in NC, which is consistent with the trend of diffuse radiation.

4.3. Response of radiation to aerosols

Four radiation parameters were calculated under the no-aerosols scenario to quantify the effect of aerosols on radiation. Fig. 5 also shows the differences in radiation caused by aerosols in China during 2001–2014. Due to the extinction of aerosols, DIRR was substantially reduced, and the annual mean loss of DIRR was −30.99 W m^{-2}. The most serious impact of aerosols on DIRR occurred in 2007, which was as much as −36.74 W m^{-2}. In contrast, the aerosols played a catalytic role in DIFR, which increased approximately 19.55%. In 2009, the increase of DIFR caused by aerosols was 17.75 W m^{-2}, accounting for 26.56% of the total diffuse radiation. Additionally, the TR and DF also separately
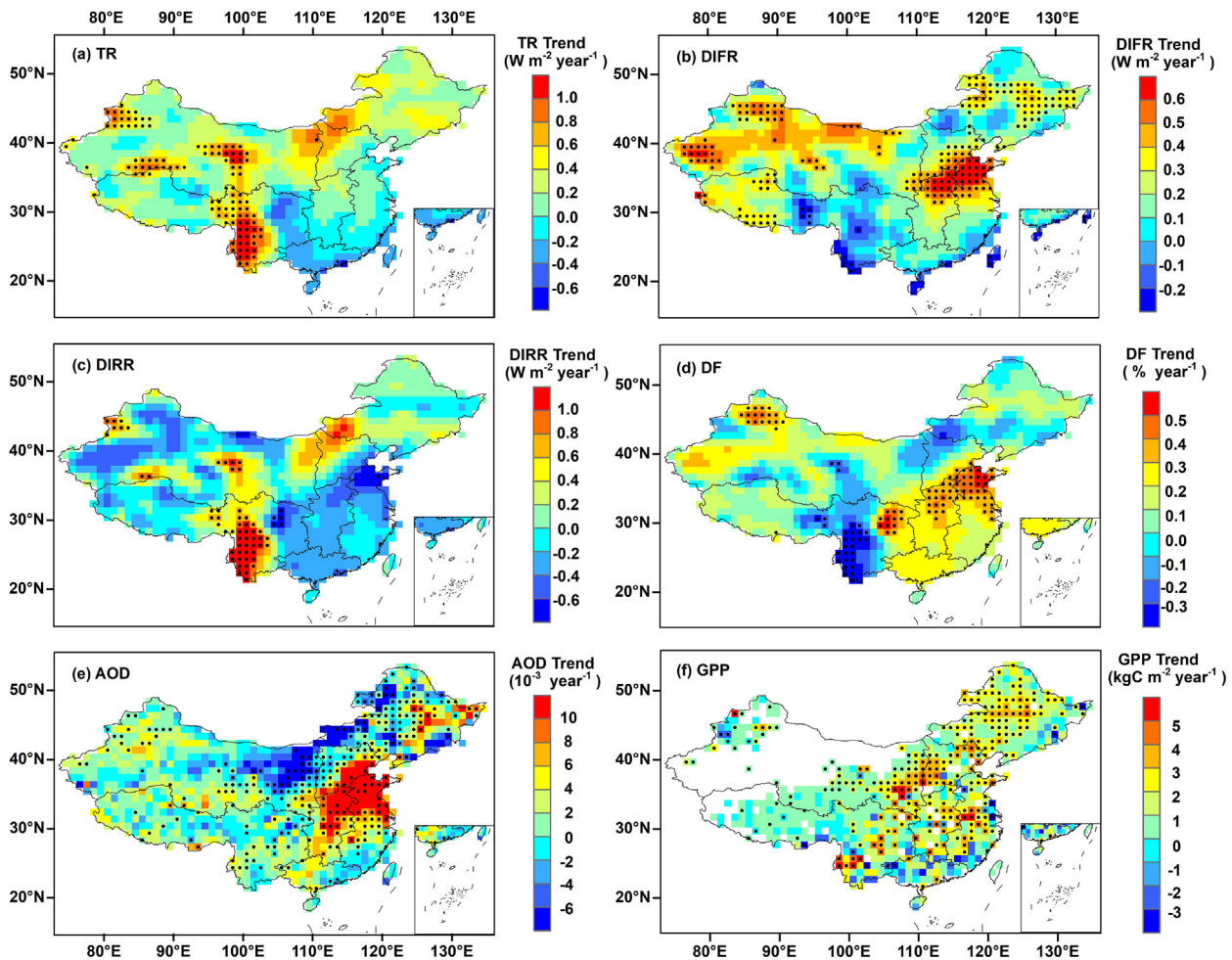
Fig. 6. The annual averaged trends for TR (a), DIFR (b), DIRR (c), DF (d), AOD (e) and GPP(f) in China from 2001 to 2014. The black dots indicate the 90% confidence level of correlation coefficient ($p < .1$).

changed -17.26 W m^{-2} and 13.43%, respectively, resulting from the impacts of the aerosols.

However, striking spatial and temporal diversities exist in China, which are caused by the differences in aerosol types and the variations in solar elevation (Yang et al., 2016). Therefore, the seasonal mean changes in radiation caused by aerosols were also calculated in the seven areas in this study and are listed in Table 2. The DIFR in the NWC region suffered the most intense positive influence by aerosols among all regions, with the annual mean DIFR increasing by 18.93 W m^{-2}, while the weakest influence occurred in the SC region, which was only 8.50 W m^{-2}. The greatest impact of aerosols on DIFR occurred in autumn for the EC, SC and CC regions, which were 16.12 W m^{-2}, 18.55 W m^{-2} and 14.14 W m^{-2}, respectively, while the influence was intense in summer for NC and NWC. The main cause of

this phenomenon was the temporal heterogeneity of dominant aerosol types in each region (Wang et al., 2011). In addition, due to agricultural production requirements, crop residue burning mainly occurred in autumn or summer, producing extensive aerosols and leading to the positive impact on DIFR in those regions (Zhang et al., 2017).

For TR, a negative influence was found in all regions, which indicated that the negative effect of aerosols on DIRR was stronger than the positive effect on DIFR. Interestingly, a significant temporal consistency was captured in China; that is, a more intense impact existed in spring and summer than in autumn and winter. Among all study areas, except for NWC (where the greatest values occurred in summer), the maximum responses of TR to aerosols all occurred in spring, in the range of -20.00 W m^{-2} (SWC) to -32.10 W m^{-2} (NC). This might be probably associated with the high solar elevation in spring and summer, which result in strong solar radiation as well as strong aerosol impacts in these two seasons. Moreover, the aerosols also caused the DF to increase significantly. The greatest impact occurred in the EC region, and the mean positive effect was 18.73%. In contrast, the NWC region showed the weakest response which was 9.43%. Generally, the aerosol-induced changes in DF were higher in autumn and winter than in spring and summer, especially in the NWC, NC, EC and CC regions, increasing 16.20% - 21.41%. Sulfur-bearing fossil fuel combustion (e.g. coal), might be the main culprit for the increase in sulfate aerosol output in the heating season (winter) in these areas, and the sulfate aerosols remaining in the atmosphere could markedly enhance the DF (Keppel and Washenfelder. 2016). Moreover, most urban agglomerations are distributed in those regions, which could cause mass emissions from

Table 1
The averaged trends of TR, DIFR, DIRR and DF in seven regions from 2001 to 2014 (* indicates $p < .1$).

Region	TR (W m^{-2} year^{-1})	DIFR (W m^2 year^{-1})	DIRR (W m^{-2} year^{-1})	DF (% year^{-1})
NEC	0.31	0.17*	0.14	0.02
NC	0.38	0.24*	0.13	0.05
EC	−0.02	0.30*	−0.31	0.27
SC	−0.26	0.04	−0.30	0.22
CC	0.05	0.34*	−0.29	0.28
NWC	0.30	0.30	−0.00	0.09
SWC	0.24	0.09	0.15	0.00

Table 2
Seasonal mean changes in radiation caused by aerosols for seven regions in China from 2001 to 2014.

Radiation	Season	NEC	NC	EC	SC	CC	NWC	SWC
TR (W m^{-2})	Spring	−20.56	−32.10	−30.68	−21.73	−28.34	−21.78	−20.00
	Summer	−15.44	−30.41	−24.84	−11.77	−24.63	−25.91	−15.85
	Autumn	−8.19	−17.06	−18.45	−14.84	−18.25	−15.90	−9.84
	Winter	−9.43	−15.64	−17.93	−13.04	−15.64	−10.71	−10.72
DIFR (W m^{-2})	Spring	12.20	17.52	12.08	2.00	9.54	19.76	9.53
	Summer	8.74	17.57	14.89	9.77	13.95	23.60	5.18
	Autumn	8.89	15.89	16.12	18.55	14.14	19.66	9.12
	Winter	11.21	14.16	12.98	11.03	10.67	12.71	10.18
DIRR (W m^{-2})	Spring	−32.76	−49.62	−42.76	−23.73	−37.88	−41.54	−36.77
	Summer	−24.18	−47.98	−39.73	−21.54	−38.58	−49.51	−35.89
	Autumn	−17.08	−32.95	−34.57	−33.39	−32.39	−35.56	−28.00
	Winter	−20.64	−29.8	−30.91	−24.07	−26.31	−23.42	−23.43
DF (%)	Spring	11.91	16.19	18.23	11.83	17.65	13.22	10.46
	Summer	8.07	16.20	15.97	9.27	15.73	14.39	7.35
	Autumn	10.47	16.20	19.30	16.95	19.45	16.23	8.84
	Winter	17.61	18.54	21.41	16.58	20.07	15.58	11.07

industrial production and residential activities, and result in high-level aerosol loadings in the atmosphere.

Furthermore, obvious differences of aerosol radiative forcing are found in the ecosystems of farmland, forest and grass in seven regions. The proportions of summertime mean changes in radiation caused by aerosols to the radiation under no-aerosol scenario were used to indicate the aerosol radiative forcing. Fig. 7 shows the aerosol radiative forcing to different ecosystems during vegetation growing season (Jun-Jul-Aug) in China. In general, the intensifying of DIFR by aerosols is lower than the weakening of DIRR, which results in the negative aerosol radiative forcing on TR. The main reason for this is that the concentration of coarse-mode aerosols (the primary causes of the loss of DIRR) is higher than that of fine-mode aerosols (Xia, 2014). However, the aerosol radiative forcing on DIRR was more significant in farmland ecosystem than other two ecosystems in most areas, especially in EC (−51.0%) and CC (−47.4%) regions. Similarly, except NEC and NC regions, the aerosol radiative forcing on DIFR in farmland was also higher than others, with the values varying from 9.7% to 20.9%, and the highest forcing on DIFR existed in grass ecosystem in NEC and NC with the values of 11.1% and 19.6%, respectively. Due to the aerosol productions by human activities, the highest negative aerosol radiative forcing occurred in farmland ecosystem in almost all regions, with the averaged forcing in China of −12.4% and varying between −5.7% - -16.7% in seven regions. Above all, aerosols show the negative radiative forcing in China ecosystems, which could also affect the physiological processes of vegetation.

4.4. Relations among the aerosol-radiation-ecosystem productivity

To investigate the impacts of aerosols on radiation for different types of ecosystem, the statistical calculations are made for the three main types of ecosystem in China from 2001 to 2014. Table S4 indicates that significant positive correlations between AOD and DIFR during autumn existed in the farmland, forest and grassland ecosystems, and the Pearson correlation coefficients R were 0.63 ($p < .05$), 0.63 ($p < .05$) and 0.69 ($p < .01$), respectively. In contrast, negative correlations existed in spring between AOD and DIFR, with correlation coefficient R values of −0.03, −0.03 and −0.10 for farmland, forest, and grassland, respectively. The correlation was also negative between AOD and TR as well as DIRR ($R < 0$) in spring for all types of ecosystem. However, the confidence coefficient p values for the negative correlations were all >0.1, indicating that the statistical significance was not achieved. The reason for this might probably be that the dominant aerosol composition for most areas of China in spring is large particles, especially coarse mode dust, which exhibited high blocking of radiation (Du et al., 2008). Moreover, with the increasing of solar elevation, the DIFR and DIRR are also increasing. Both of them have been proved to be a functional relationship (Soler, 1988). Therefore, the differences in solar elevation could also lead to uncertainties in the relationship among AOD-radiation. Fig. 8 shows the relationships between the aerosol and DF for farmland, forest and grass ecosystem in China for different seasons during 2001–2014. In spring, a significant positive effect was captured for the farmland ecosystem in the NEC and SC regions, with correlation coefficients R of
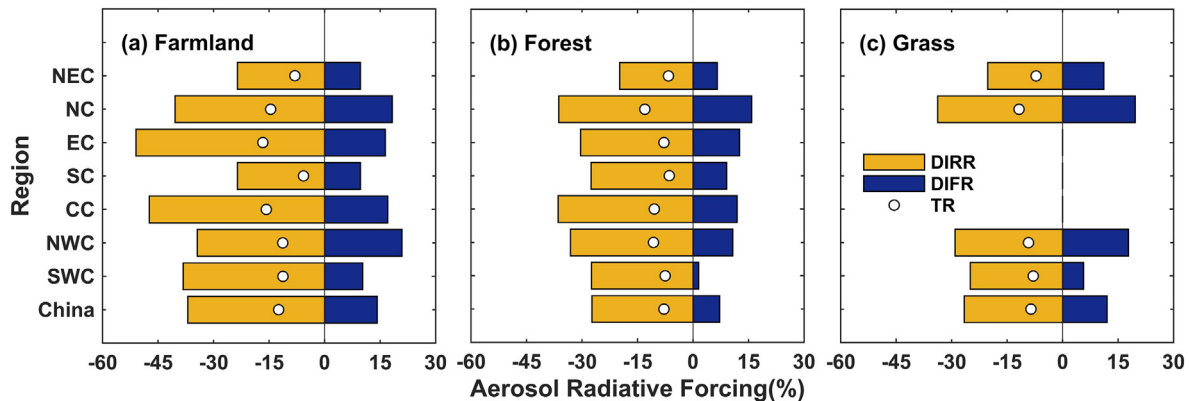

Fig. 7. The averaged aerosol radiative forcing of TR (circle), DIFR (blue bar) and DIRR (orange bar) for ecosystem of farmland, forest and grass during vegetation growing season (Jun-Jul-Aug). (For interpretation of the references to colour in this figure legend, the reader is referred to the web version of this article.)

0.73 ($p < .01$) and 0.83 ($p < .01$). For the forest ecosystem, this effect existed in the NEC, NC and SC regions, and the R values were 0.68 (<0.01), 0.53 ($p < .05$) and 0.63 ($p < .05$), respectively. However, a significant negative effect was found in the grass ecosystem for NWC ($R = -0.56$, $p < .05$), which was mainly due to the strong extinction caused by dust during this phase. In contrast, a positive correlation existed in the SWC and NEC grass ecosystem regions, with R values of 0.54 ($p < .05$) and 0.79 ($p < .01$). During summer, except for the farmland and forest ecosystems in SWC (statistical significance not achieved), positive correlations between AOD and DF were widespread in all ecosystems in China. The highest R value occurred in the EC farmland regions ($R = 0.85$, $p < .01$). The DF in the EC forest region also possessed a high correlation with aerosol, with R of 0.83 ($p < .01$). Furthermore, obvious positive impacts of aerosol on DF existed among the main ecosystems of China in the autumn and winter, except the SC farmland ecosystem for autumn and the NEC forest and grassland ecosystem for winter. The correlation coefficients R in the farmland, forest and grass ecosystems were in the range of 0.27–0.81, 0.12–0.60 and 0.41–0.61, respectively for autumn, and 0.11–0.79, 0.05–0.83 and 0.49–0.69, respectively for winter. Apart from the influence of aerosol, other factors, e.g., cloud cover, altitude, slope and aspect, may also cause radiation changes, which we could consider in future research.

Aerosol can indirectly affect vegetation productivity (e.g. GPP) by modifying radiation; therefore, the correlation coefficients between AOD and GPP were also calculated to understand the extent by which the aerosols influence ecosystems of different types for different seasons. Fig. 9 shows the spatial distribution of seasonal Pearson correlation coefficients in seven areas from 2001 to 2014. Noticeably, the retrieval of AOD and GPP are both affected by surface albedo, in our paper the highest quality AOD and GPP products are used, which

could eliminate the influence of surface albedo on the two variables in the greatest extent. It is clear that aerosols imposed significant negative effects on GPP in the eastern area of NWC, which were mainly caused by the extinction of dust aerosols for all season. In contrast, only a few regions exhibited a significant positive correlation, e.g., the eastern areas of SWC and NEC, which are characterized with high forest coverage. This phenomenon was related to the increasing DIFR, which results in the enhanced effect of diffuse fertilization.

In the growing season of vegetation (most in summer), increased air humidity would result in high AOD as well as high cloud cover, which would in turn decrease the TR in most areas of SC, and thus there existed a negative correlation between AOD and GPP. Similar to spring, the forests in eastern SWC and NEC appeared to exhibit the diffuse fertilization effect. Approximately 18.6% of areas in China showed significant correlation between AOD and GPP ($p < .1$) in autumn, among which negative correlation accounts for 65.1% and positive correlation for 34.9%. The correlations did not achieve statistical significance in most areas of China, where the vegetation photosynthesis was limited by other environmental variables, i.e., temperature, water and CO_2 concentration. In winter, several aerosol pollution episodes occurred in China from 2001 to 2014, and the influence of aerosols on GPP was generally more intense than other seasons. Approximately 15.1% of the areas showed significant negative correlation, and the negative correlation was mainly concentrated in eastern NWC and NC region. The absorption of light by aerosols could reduce the total radiation, thus reducing vegetation light utilization.

Photosynthetic efficiency plays an important role in the spatial distribution for the relationships of aerosol-GPP, and it mainly depends on the leaf area index and canopy structure of vegetation. Therefore, the correlation coefficient R was also separately calculated in farmland,
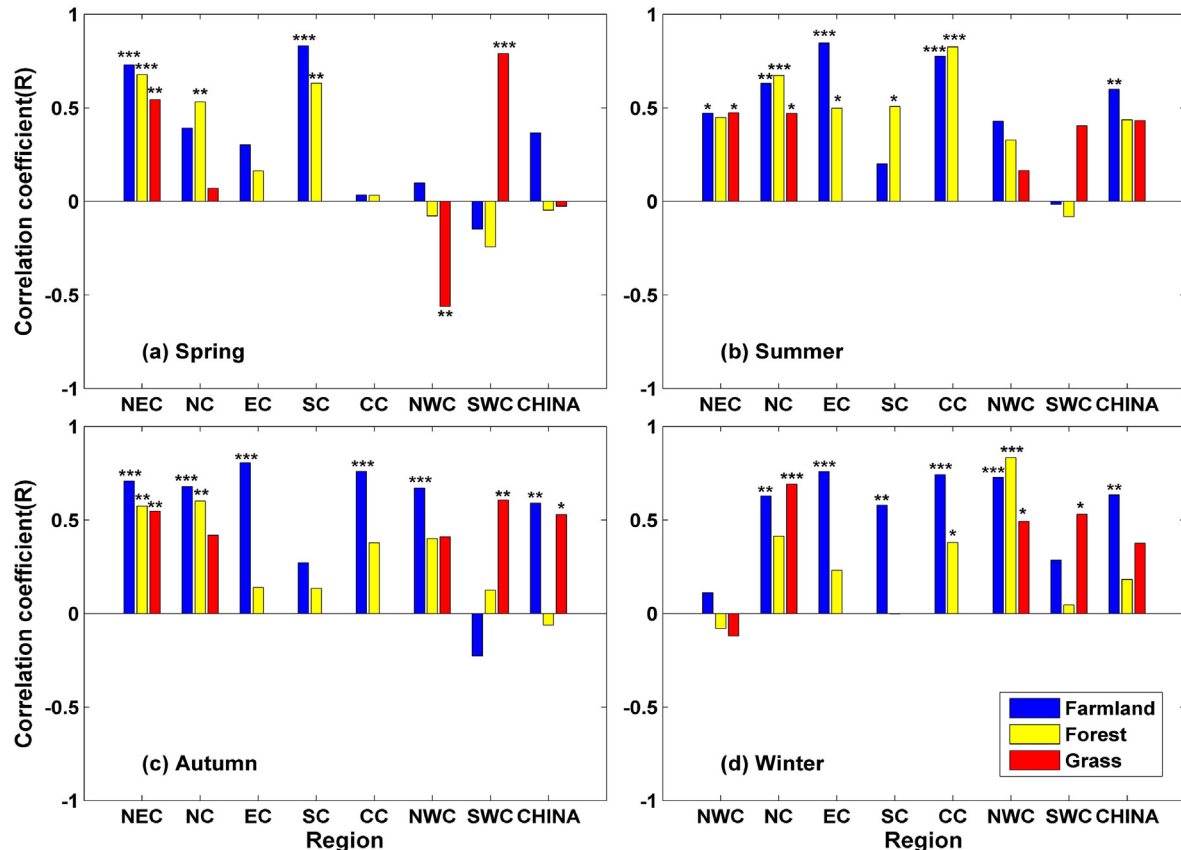

Fig. 8. The seasonal Pearson correlation coefficients of aerosol-DF for three ecosystems in China from 2001 to 2014: (a) Spring; (b) Summer; (c) Autumn and (d) Winter, where *,**,*** indicate the confidence coefficients at the 90%, 95% and 99% levels, respectively.
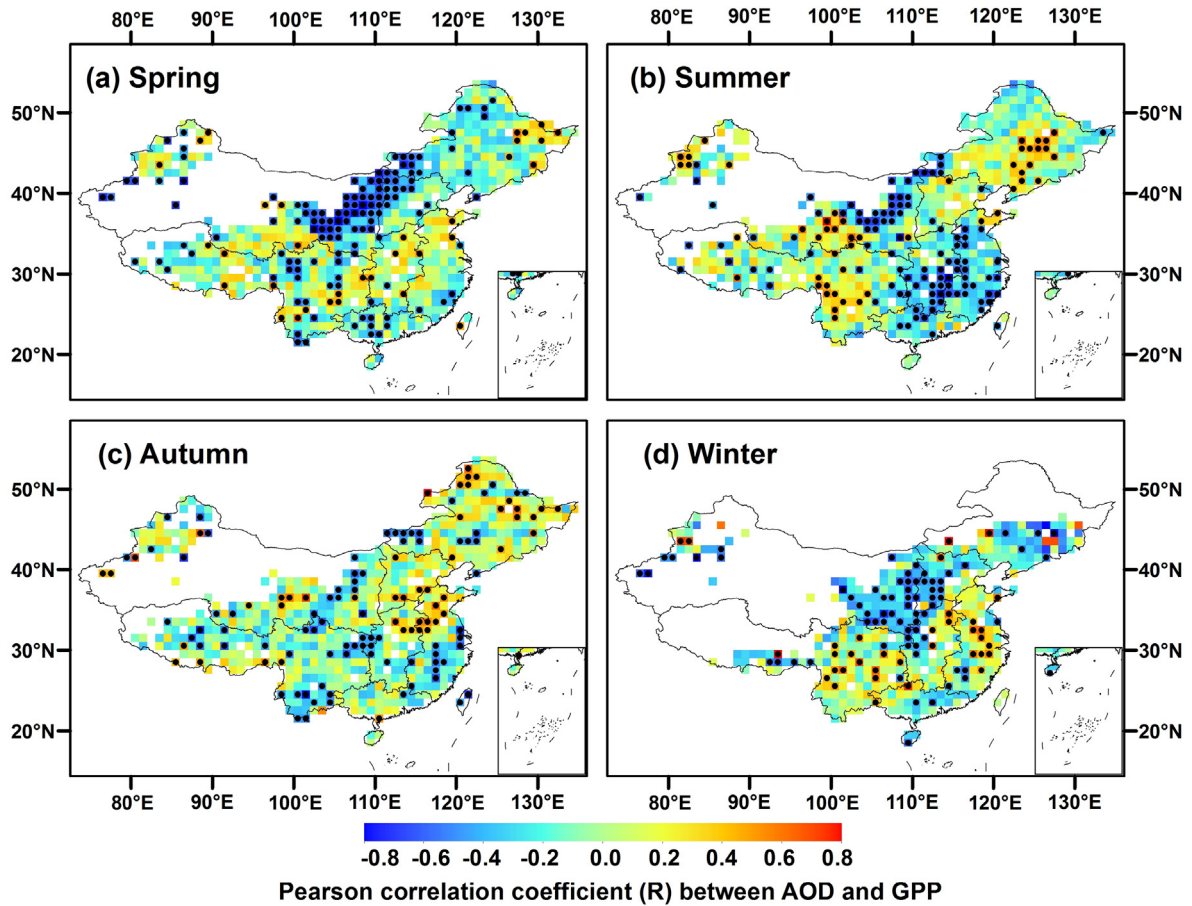
Fig. 9. The spatial distributions of seasonal Pearson correlation coefficients between AOD and GPP in China during 2001–2014. The black dots indicate the significance level of 90%.

forest and grass ecosystems in China. In addition, to exclude the restriction of temperature and CO_2 concentrations on photosynthesis, the correlation between AOD and GPP was only collected in the growing season of vegetation (Jun-Aug). Fig. 10 shows the Pearson correlation coefficients R of AOD-GPP for three ecosystems in China during the growing season of vegetation. Although the negative effects ($R < 0$) were widespread in China, the confidence levels did not all achieve statistical significance ($p > .1$). The limitation of water and nutrients such as nitrogen and phosphorus in this season could also influence the relationship of aerosol-GPP. Furthermore, the farmland ecosystems were mostly established by human activities (Dai et al., 2020; Yao et al.,

2019), in which was involved large human interference, and the relationship of aerosol-GPP was thus non-significant. For forest ecosystems in EC and CC, there existed significant negative impacts of AOD on GPP, with the correlation coefficients R of −0.59 ($p < .05$) and − 0.76 ($p < .01$), respectively. Although the diffuse fertilization effect could cause the increase of GPP, especially for the canopy vegetation, the loss of direct radiation was higher, and it might eventually lead to a reduction in the total GPP. In contrast, the R value was 0.24 ($p > .1$) in the SWC region, where was characterized with low levels of aerosols. The negative effects of aerosols on GPP occurred in all of China in the grass ecosystem, and the strongest effect occurred in NWC (R = -0.46,
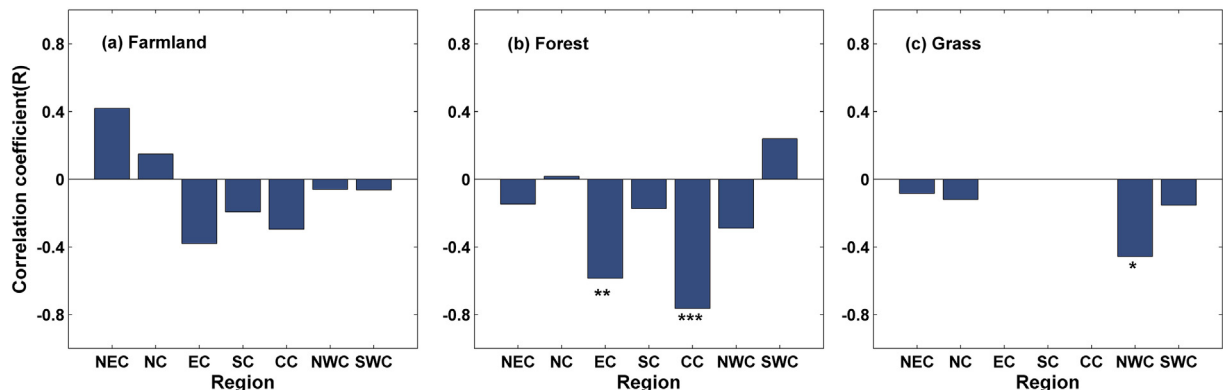

Fig. 10. The relationships between AOD and GPP for farmland (a), forest (b) and grass (c) ecosystems during the growing season of vegetation in seven regions from 2001 to 2014.

$p < .1$). This suggests that high level aerosols could play a negative role in the photosynthesis of farmland, forest and grass ecosystems in most areas of China.

5. Conclusions

The spatiotemporal variations and relationships of aerosol-radiation-ecosystem productivity in China for 2001–2014 were discussed and analyzed in this paper. For this purpose, a radiative transfer model (Fu-Liou model) was selected to simulate the network of history radiation. The simulated results show excellent consistency compared with in situ measured radiation data, with the correlation coefficient R^2 (RMSE, MAE) of 0.88 (18.12 $\mathrm{W\,m^{-2}}$, 21.35 $\mathrm{W\,m^{-2}}$) and 0.79 (14.40 $\mathrm{W\,m^{-2}}$, 11.49 $\mathrm{W\,m^{-2}}$), respectively.

From 2001 to 2014, a significant increasing trend was captured in diffuse radiation in China, which was 0.22 $\mathrm{W\,m^{-2}}$ per year, especially in central China where the upward trend was 0.34 $\mathrm{W\,m^{-2}\,year^{-1}}$. In addition, the diffuse factor also increased in this phase for most areas, with trends of 0.00%–0.28% $\mathrm{year^{-1}}$. However, the radiation trend under no-aerosol scenario indicated that although the aerosols increase the uptrend of diffuse radiation, it could relieve the brightening trend in China due to the weakening of direct radiation by aerosols. In this period, the aerosol optical depth (AOD) increased at a rate of approximately 0.002 $\mathrm{year^{-1}}$. Quantified analysis also shows that aerosols caused the mean diffuse radiation to increase 13.73 $\mathrm{W\,m^{-2}}$, and total radiation and direct radiation to decrease 17.26 $\mathrm{W\,m^{-2}}$ and 30.99 $\mathrm{W\,m^{-2}}$, respectively, in China.

Spatiotemporal variations of aerosol radiative forcing existed for different ecosystems in China, which can also cause the heterogeneity of aerosol-GPP relationship, and those features were captured in our study. It was found that a significant negative correlation between AOD and GPP existed in the forest ecosystems of eastern and central China during the growing season of vegetation. Although aerosols can cause diffuse fertilization effects on canopy vegetation, the growth of vegetation might still be restrained because of reduced radiation by high level of aerosols in this area. Fortunately, with the proposal of an air pollution control action plan in China in 2013, the air pollution has been effectively controlled, which shows a profound significance for the improvement of ecosystem productivity.

CRediT authorship contribution statement

Wenhao Xue: Writing - original draft, Formal analysis. **Jing Zhang:** Conceptualization, Formal analysis. **Yan Qiao:** Data curation, Formal analysis. **Jing Wei:** Data curation, Formal analysis. **Tianwei Lu:** Formal analysis. **Yunfei Che:** Formal analysis. **Yulu Tian:** Formal analysis.

Declaration of competing interest

All authors declare no conflict of interest.

Acknowledgments

Appendix A. Supplementary data

Supplementary data to this article can be found online at https://doi.org/10.1016/j.scitotenv.2020.140324.

References

Andreae, M.O., Rosenfeld, D., 2008. Aerosol-cloud-precipitation interactions. Part 1. The nature and sources of cloud-active aerosols. Earth Sci. Rev. 89, 13–41.

Bassani, C., Manzo, C., Zakey, A., et al., 2016. Effect of the aerosol type selection for the retrieval of shortwave ground net radiation: case study using Landsat 8 data. Atmosphere 7, 111.

Chan, C.K., Yao, X., 2008. Air pollution in mega cities in China. Atmos. Environ. 42, 1–42.

Chandra, S., Satheesh, S.K., Srinivasan, J., 2004. Can the state of mixing of black carbon aerosols explain the mystery of 'excess' atmospheric absorption? Geophys. Res. Lett. 31.

Che, H., Zhang, X., Li, Y., et al., 2007. Horizontal visibility trends in China 1981–2005. Geophys. Res. Lett. 34, L24706.

Chen, X., Wang, L., Niu, Z., et al., 2020. The effects of projected climate change and extreme climate on maize and rice in the Yangtze River Basin, China. Agricultural Forest Meteorology 282–283 107867.

Cheng, S.J., Bohrer, G., Steiner, A.L., et al., 2015. Variations in the influence of diffuse light on gross primary productivity in temperate ecosystems. Agricultural Forest Meteorology 201, 98–110.

Dai, X., Wang, L., Huang, C., et al., 2020. Spatio-temporal variations of ecosystem services in the urban agglomerations in the middle reaches of the Yangtze River, China. Ecol. Indic. 115, 106394.

Ding, Y., Ren, G., Shi, G., 2007. China's national assessment report on climate change(summary). World Environment 3, 1–5.

Doelling, D.R., Loeb, N.G., Keyes, D.F., et al., 2013. Geostationary enhanced temporal interpolation for CERES flux products. Journal of Atmospheric Oceanic Technology 30, 1072–1090.

Du, W., Xin, J., Wang, M., et al., 2008. Photometric measurements of spring aerosol optical properties in dust and non-dust periods in China. Atmos. Environ. 42, 7981–7987.

Fan, J., Chen, B., Wu, L., et al., 2018. Evaluation and development of temperature-based empirical models for estimating daily global solar radiation in humid regions. Energy 144, 903–914.

Fan, J., Wu, L., Zhang, F., et al., 2019. Empirical and machine learning models for predicting daily global solar radiation from sunshine duration: a review and case study in China. Renewable Sustainable Energy Reviews 100, 186–212.

Gelaro, R., Mccarty, W., Suarez, M.J., et al., 2017. The modern-era retrospective analysis for research and applications, version 2 (MERRA-2). J. Clim. 30, 5419–5454.

Gu, L., Baldocchi, D.D., Wofsy, S.C., et al., 2003. Response of a deciduous forest to the Mount Pinatubo eruption: enhanced photosynthesis. Science 299, 2035–2038.

Guo, J., Zhang, X., Wu, Y., et al., 2011. Spatio-temporal variation trends of satellite-based aerosol optical depth in China during 1980–2008. Atmos. Environ. 45, 6802–6811.

Hsu, N.C., Jeong, M., Bettenhausen, C., et al., 2013. Enhanced deep blue aerosol retrieval algorithm: the second generation. J. Geophys. Res. 118, 9296–9315.

Hsu, N.C., Lee, J., Sayer, A.M., et al., 2019. VIIRS deep blue aerosol products over land: extending the EOS long-term aerosol data records. J. Geophys. Res. 124, 4026–4053.

Huang, J., Fu, Q., Su, J., et al., 2009. Taklimakan dust aerosol radiative heating derived from CALIPSO observations using the Fu-Liou radiation model with CERES constraints. Atmos. Chem. Phys. 9, 4011–4021. https://doi.org/10.5194/acp-9-4011-2009.

Jiang, W., Wang, L., Feng, L., et al., 2019. Drought characteristics and its impact on changes in surface vegetation from 1981 to 2015 in the Yangtze River Basin, China. Int. J. Climatol. 40 (7), 3380–3397.

Kalnay, E., Kanamitsu, M., Kistler, R., et al., 1996. The NCEP/NCAR 40-year reanalysis project. Bull. Am. Meteorol. Soc. 77, 437–471.

Kaplan, A.G., Kaplan, Y.A., 2020. Developing of the new models in solar radiation estimation with curve fitting based on moving least-squares approximation. Renew. Energy 146, 2462–2471.

Kato, S., Rose, F.G., Charlock, T.P., 2005. Computation of domain-averaged irradiance using satellite-derived cloud properties. Journal of Atmospheric Oceanic Technology 22, 146–164.

Keppelaleks, G., Washenfelder, R.A., 2016. The effect of atmospheric sulfate reductions on diffuse radiation and photosynthesis in the United States during 1995–2013. Geophys. Res. Lett. 43, 9984–9993.

Levy, R.C., Remer, L.A., Kleidman, R.G., et al., 2010. Global evaluation of the collection 5 MODIS dark-target aerosol products over land. Atmospheric Chemistry Physics 10, 10399–10420.

Li, C., I, J., Dubovik, O., et al., 2020. Remote sensing impact of aerosol vertical distribution on aerosol optical depth retrieval from passive satellite sensors. Remote Sens. 12.

Mahowald, N.M., Ward, D.S., Kloster, S., et al., 2011. Aerosol impacts on climate and biogeochemistry. Annual Review of Environment Resources 36, 45–74.

Moazenzadeh, R., Mohammadi, B., Shamshirband, S., et al., 2018. Coupling a firefly algorithm with support vector regression to predict evaporation in Northern Iran. Engineering Applications of Computational Fluid Mechanics 12, 584–597.

Niyogi, D., Chang, H., Saxena, V.K., et al., 2004. Direct observations of the effects of aerosol loading on net ecosystem CO2 exchanges over different landscapes. Geophysical Research Letter 31.

Osullivan, M., Rap, A., Reddington, C.L., et al., 2016. Small global effect on terrestrial net primary production due to increased fossil fuel aerosol emissions from East Asia since the turn of the century. Geophys. Res. Lett. 43, 8060–8067.

Penner, E.J., Chuang, C.C., Grant, K.E., 1998. Climate forcing by carbonaceous and sulfate aerosols. Clim. Dyn. 14, 839–851.

Pinty, B., Lattanzio, A., Martonchik, J.V., et al., 2005. Coupling diffuse sky radiation and surface albedo. J. Atmos. Sci. 62, 2580–2591.

Qu, S., Wang, L., Lin, A., et al., 2020. Distinguishing the impacts of climate change and anthropogenic factors on vegetation dynamics in the Yangtze River Basin, China. Ecol. Indic. 108, 105724.

Rap, A., Scott, C.E., Reddington, C.L., et al., 2018. Enhanced global primary production by biogenic aerosol via diffuse radiation fertilization. Nat. Geosci. 11, 640–644.

Running, Steve, Qiaozhen Mu - University of Montana, Maosheng Zhao - University of Maryland, MODAPS SIPS - NASA, 2015. MOD17A2H MODIS/Terra Gross Primary Productivity 8-Day L4 Global 500m SIN Grid. NASA LP DAAC. https://doi.org/10.5067/MODIS/MOD17A2H.006.

Sayer, A.M., Hsu, N., Lee, Christina, et al., 2019. Validation, stability, and consistency of MODIS collection 6.1 and VIIRS version 1 deep blue aerosol data over land. J. Geophys. Res. 124, 4658–4688.

Sayer, A.M., Munchak, L.A., Hsu, N.C., et al., 2014. MODIS collection 6 aerosol products: comparison between aqua's e-deep blue, dark target, and "merged" data sets, and usage recommendations. J. Geophys. Res.

Schaaf, C.B., Gao, F., Strahler, A.H., et al., 2002. First operational BRDF, albedo nadir reflectance products from MODIS. Remote Sens. Environ. 83, 135–148.

Soler, A., 1988. The dependence on solar elevation of the correlation between monthly average hourly diffuse and global radiation. Sol. Energy 41, 335–340.

Stocker, T.F., Qin, D., Plattner, G.K., et al., 2013. IPCC, 2013: climate change 2013: the physical science basis. Contribution of working group I to the fifth assessment report of the intergovernmental panel on climate change. Comput. Geom. 18, 95–123.

Tang, W., Yang, K., Qin, J., et al., 2011. Solar radiation trend across China in recent decades: a revisit with quality-controlled data. Atmospheric Chemistry Physics 11, 393–406.

Tie, X., Cao, J., 2009. Aerosol pollution in China: present and future impact on environment. Particuology 7, 426–431.

Unger, N., Yue, X., Harper, K., 2017. Aerosol climate change effects on land ecosystem services. Faraday Discuss. 200, 121–142.

Wang, Y., Wild, M., 2016. A new look at solar dimming and brightening in China. Geophysical Research Letter 43.

Wang, Y., Xin, J., Li, Z., et al., 2011. Seasonal variations in aerosol optical properties over China. J. Geophys. Res. 116.

Wei, J., Huang, B., Sun, L., Zhang, Z., Wang, L., Bilal, M., 2017. A simple and universal aerosol retrieval algorithm for Landsat series images over complex surfaces. J. Geophys. Res. 122 (24), 13338–13355.

Wei, J., Sun, L., Peng, Y., et al., 2018. An improved high-spatial-resolution aerosol retrieval algorithm for MODIS images over land. J. Geophys. Res. 123.

Wei, J., Peng, Y., Guo, J., et al., 2019a. Performance of MODIS collection 6.1 level 3 aerosol products in spatial-temporal variations over land. Atmos. Environ. 206, 30–44.

Wei, J., Peng, Y., Mahmood, R., et al., 2019b. Intercomparison in spatial distributions and temporal trends derived from multi-source satellite aerosol products. Atmos. Chem. Phys. 19, 7183–7207.

Wei, J., Li, Z., Peng, Y., et al., 2019c. MODIS collection 6.1 aerosol optical depth products over land and ocean: validation and comparison. Atmos. Environ. 201, 428–440.

Wei, J., Li, Z., Peng, Y., et al., 2019d. A regionally robust high-spatial-resolution aerosol retrieval algorithm for MODIS images over eastern China. IEEE Trans. Geosci. Remote Sens. 57, 4748–4757.

Wei, J., Huang, W., Li, Z., et al., 2019e. Estimating 1-km-resolution PM2.5 concentrations across China using the space-time random forest approach. Remote Sens. Environ. 231, 111221. https://doi.org/10.1016/j.rse.2019.111221.

Wei, J., Li, Z., Guo, J., et al., 2019f. Satellite-derived 1-km-resolution PM1 concentrations from 2014 to 2018 across China. Environ. Sci. Technol. 53, 13265–13274.

Wei, J., Li, Z., Maureen, C., et al., 2020. Improved 1 km resolution PM2.5 estimates across China using enhanced space-time extremely randomized trees. Atmos. Chem. Phys. 20, 3273–3289.

Williams, I.N., Riley, W.J., Kueppers, L.M., et al., 2016. Separating the effects of phenology and diffuse radiation on gross primary productivity in winter wheat. J. Geophys. Res. 121, 1903–1915.

Xia, X., 2014. A critical assessment of direct radiative effects of different aerosol types on surface global radiation and its components. Journal of Quantitative Spectroscopy Radiative Transfer 149, 72–80.

Xue, W., Zhang, J., Zhong, C., et al., 2020. Satellite-derived spatiotemporal PM2.5 concentrations and variations from 2006 to 2017 in China. Sci. Total Environ. 712.

Yang, X., Zhao, C., Zhou, L., et al., 2016. Distinct impact of different types of aerosols on surface solar radiation in China. J. Geophys. Res. 121, 6459–6471.

Yao, R., Wang, L., Huang, X., et al., 2019. Greening in rural areas increases the surface urban Heat Island intensity. Geophys. Res. Lett. 46, 2204–2212.

Yue, X., Unger, N., 2018. Fire air pollution reduces global terrestrial productivity. Nat. Commun. 9, 5413.

Yue, X., Strada, S., Unger, N., et al., 2017. Future inhibition of ecosystem productivity by increasing wildfire pollution over boreal North America. Atmospheric Chemistry Physics 17, 13699–13719.

Zhang, X., Xia, X., Xuan, C., 2015. On the drivers of variability and trend of surface solar radiation in Beijing metropolitan area. Int. J. Climatol. 35, 452–461.

Zhang, H., Hu, J., Qi, Y., et al., 2017. Emission characterization, environmental impact, and control measure of PM2.5 emitted from agricultural crop residue burning in China. J. Clean. Prod. 149, 629–635.

Zhang, M., Wang, Y., Ma, Y., et al., 2018. Spatial distribution and temporal variation of aerosol optical depth and radiative effect in South China and its adjacent area. Atmos. Environ. 188, 120–128.

Zhang, J., Ding, J., Zhang, J., et al., 2020a. Effects of increasing aerosol optical depth on the gross primary productivity in China during 2000–2014. Ecol. Indic. 108.

Zhang, W., Wang, L., Xiang, F., et al., 2020b. Vegetation dynamics and the relations with climate change at multiple time scales in the Yangtze River and Yellow River Basin, China. Ecol. Indic. 110.

Zhou, Z., Wang, L., Lin, A., et al., 2018. Innovative trend analysis of solar radiation in China during 1962–2015. Renew. Energy 119, 675–689.

Zou, L., Lin, A., Wang, L., et al., 2016. Long-term variations of estimated global solar radiation and the influencing factors in Hunan province, China during 1980–2013. Meteorology Atmospheric Physics 128, 155–165.